**Correspondence to:**
W. Wang,
wbwang@ucar.edu

# Physical Processes Driving the Response of the $F_2$ Region Ionosphere to the 21 August 2017 Solar Eclipse at Millstone Hill

Wenbin Wang[1], Tong Dang[2], Jiuhou Lei[2], Shunrong Zhang[3], Binzheng Zhang[1], and Alan Burns[1]

[1]High Altitude Observatory, National Center for Atmospheric Research, Boulder, CO, USA, [2]CAS Key Laboratory of Geospace Environment, School of Earth and Space Sciences, University of Science and Technology of China, Hefei, China, [3]MIT Haystack Observatory, Westford, MA, USA

**Abstract** The high-resolution thermosphere-ionosphere-electrodynamics general circulation model has been used to investigate the response of $F_2$ region electron density (Ne) at Millstone Hill (42.61°N, 71.48°W, maximum obscuration: 63%) to the Great American Solar Eclipse on 21 August 2017. Diagnostic analysis of model results shows that eclipse-induced disturbance winds cause $F_2$ region Ne changes directly by transporting plasma along field lines, indirectly by producing enhanced O/N$_2$ ratio that contribute to the recovery of the ionosphere at and below the $F_2$ peak after the maximum obscuration. Ambipolar diffusion reacts to plasma pressure gradient changes and modifies Ne profiles. Wind transport and ambipolar diffusion take effect from the early phase of the eclipse and show strong temporal and altitude variations. The recovery of $F_2$ region electron density above the $F_2$ peak is dominated by the wind transport and ambipolar diffusion; both move the plasma to higher altitudes from below the $F_2$ peak when more ions are produced in the lower $F_2$ region after the eclipse. As the moon shadow enters, maximizes, and leaves a particular observation site, the disturbance winds at the site change direction and their effects on the $F_2$ region electron densities also vary, from pushing plasma downward during the eclipse to transporting it upward into the topside ionosphere after the eclipse. Chemical processes involving dimming solar radiation and changing composition, wind transport, and ambipolar diffusion together cause the time delay and asymmetric characteristic (fast decrease of Ne and slow recovery of the eclipse effects) of the topside ionospheric response seen in Millstone Hill incoherent scatter radar observations.

## 1. Introduction

A solar eclipse provides a unique opportunity of active experiment of solar radiation effects on the photochemistry, dynamics, and energetics of the coupled ionosphere-thermosphere (I-T) system. The short duration of the decrease or absence of solar radiation temporally reduces both the heating to the upper atmosphere and the ionization as a source for the ionosphere. The localized, rapid decreases and quick recovery of solar radiation during an eclipse do not simply resemble sunset and sunrise in the upper atmosphere but generate a unique transient, dynamic state in the moon shadow region that moves rapidly along the eclipse path. The study of the eclipse effects on the I-T system has long been the focus of ionospheric research for not only morphologically describing the eclipse effects but also exploring the physical processes that govern the I-T system response to changing driving conditions of different temporal and spatial scales (e.g.,Ledig et al., 1946; Rishbeth, 1968).

Observations of the eclipse effects on the I-T system have been primarily on ionospheric changes, as neutral parameters are very difficult to observe during the short transient period of a solar eclipse. TEC maps from GPS receivers and ionosonde data are the primary data sources for eclipse effect studies (e.g.,Adekoya & Chukwuma, 2016; Afraimovich et al., 1998, 2002, 2007; Cherniak & Zakharenkova, 2018; Coster et al., 2017; Ding et al., 2010; Farges et al., 2001; Korenkov et al., 2003; Kurkin et al., 2001; Le et al., 2008; Tsai & Liu, 1999; Zhang et al., 2017). Incoherent scatter radars (ISRs) have also been used to study eclipse effects (e.g., Baron & Hunsucker, 1973, Burmaka & Chernogor, 2013, Domnin et al., 2013, Evans, 1965a, 1965b, Grigorenko et al., 2008, Pitout et al., 2013, Salah et al., 1986). ISRs have the advantage of measuring multiple key ionospheric parameters simultaneously and have good temporal and vertical coverage, although eclipse

events occurring right over the radar sites are rare. Previous observations show that the ionospheric response to a solar eclipse is a dynamic and complicated one.

To understand this response requires a full, self-consistent treatment of not only the photochemistry and ionospheric plasma diffusion along magnetic field lines that are affected directly by solar radiation change during an eclipse but also the dynamic transport of ionization by electric fields, as well as the interaction between the ionosphere and thermosphere (e.g., Adekoya & Chukwuma, 2016, Huba & Drob, 2017, Le et al., 2008). This treatment, however, has not been able to be realized until now. For instance, using a thermosphere model, Ridley et al. (1984) showed that neutral winds, composition, and temperature could undergo substantial changes during an eclipse. Similar thermospheric model results were also used by Roble et al. (1986) to simulate the ionospheric response to an annular eclipse and to compare model results with Millstone Hill ISR observations. The effects of an eclipse on the thermosphere and ionosphere were also simulated by Müller-Wodarg et al. (1998). These early theoretical studies, however, did not self-consistently solve the I-T system with fully coupled chemistry, dynamics, energetics, and electrodynamics. The eclipse-induced wind and ionospheric conductivity changes and their impacts on the I-T system through electrodynamics (e.g., Madhav Haridas & Manju, 2012; Shweta Sharma et al., 2010) were not fed back to the ionospheric models to affect the modeled ionosphere during eclipses.

Furthermore, most of the theoretical studies of ionospheric responses to eclipses have used empirical models of the thermosphere, such as the MSIS model (Picone et al., 2002), to specify the neutral parameters for ionospheric inputs (e.g., Boitman et al., 1999, Le et al., 2008, 2009, 2010, Lyashenko & Chernogor, 2013, Pitout et al., 2013); thus, the dynamic coupling between the neutral atmosphere and the ionosphere during eclipses was not self-consistently simulated. The models used were also of coarse resolution that could not fully resolve the transient and detailed structures associated with eclipses. In addition, most of these early theoretical studies were descriptive and have not made a quantitative and systematic analysis of the physical processes driving the eclipse effects and their temporal and spatial variations that are seen in the observations (Cherniak & Zakharenkova, 2018).

In this paper, we use the high-resolution Thermosphere Ionosphere Electrodynamics General Circulation Model (TIEGCM) to uncover the physical processes that drive the temporal and spatial variations of ionospheric $F$ region eclipse effects by performing diagnostic analysis of the model outputs and comparing with Millstone Hill ISR observations during the 21 August 2017 Great American Solar Eclipse. We also use this analysis to elucidate, for the first time, the temporal and altitudinal changes of the relative contribution of each process, including chemistry, winds, ambipolar diffusion, and transport by electric fields, to $F$ region ionospheric eclipse effects over the course of the eclipse. Specifically, the effects of the time delay between the maximum local obscuration and the maximum $F$ region electron density depletion and asymmetry around an eclipse have long been observed; the physical processes causing these effects have been postulated by other researchers (e.g., Rishbeth, 1968, Stubbe, 1970) but have not been fully resolved in the context of a coupled I-T system—this is one of the main goals of this paper.

## 2. Methodology

The Millstone Hill ISR conducted 5-day observations centered on 21 August 2017. In this study, we used the zenith antenna data of electron density (Ne) profiles from interleaved 480-μs single pulse measurements above 250 km (black solid squares in Figures 1c–1f) and alternating code measurements below 250 km (gray solid circles in Figures 1c–1f). This allows for appropriate data quality in different altitude ranges. We have calibrated ISR Ne against the digisonde data.

The TIEGCM solves time-dependent momentum, energy, and continuity equations for the neutrals and energy and continuity equations for the ions of the coupled I-T system on a global grid (Qian et al., 2014; Richmond et al., 1992; Roble et al., 1988). Recently, the TIEGCM V2.0 has been upgraded to high resolution with a 0.625° × 0.625° geographic latitude-longitude grid and 1/4 scale height in the vertical pressure coordinates to facilitate the simulation of small-scale and mesoscale processes in the I-T system. In this study, this high-resolution version of the model is used as it better describes the structures and variations caused by the solar eclipse than previous versions of the model (Dang, Lei, Wang, Burns, et al., 2018; Dang, Lei, Wang, Zhang, et al., 2018).
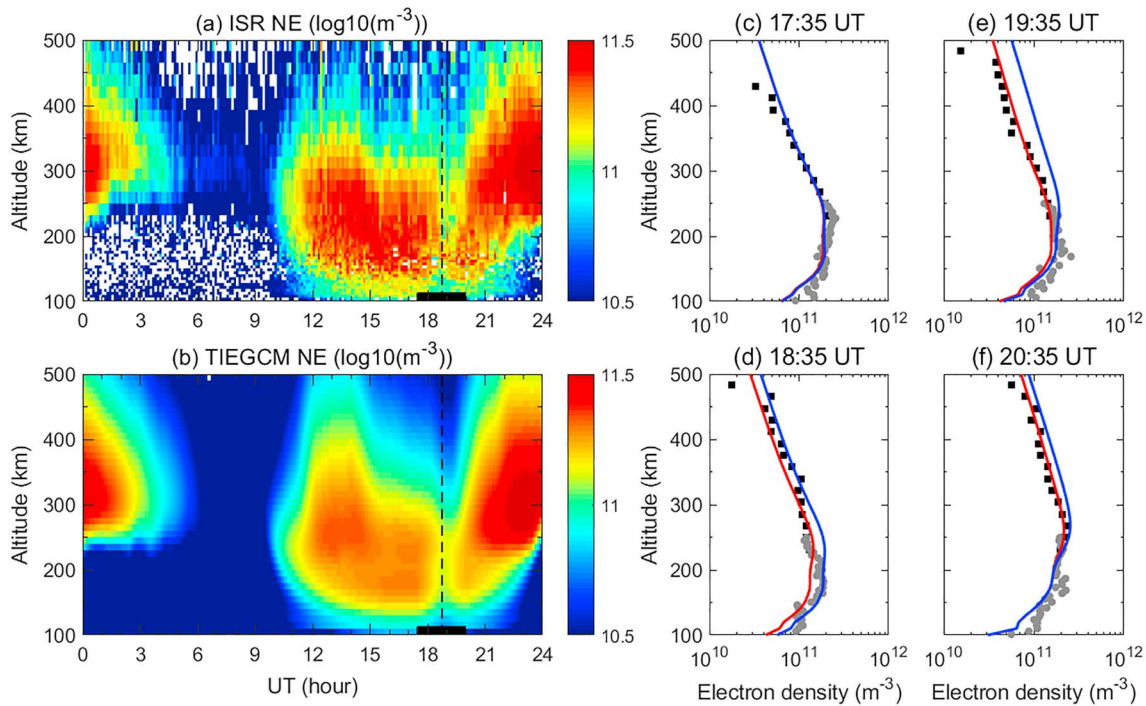
**Figure 1.** UT and altitude variations of electron densities from (a) incoherent scatter radar observations and (b) TIEGCM simulations at Millstone Hill on 21 August 2017. The vertical dashed lines show the time of maximum eclipse at the location; the horizontal bars indicate the duration of the eclipse. (c–f) Give electron density profiles from observations (black squares are observations from interleaved single pulse measurements above 250 km, and gray dots are from alternating code observations below 250 km) and model simulations with the eclipse (red) and without the eclipse (blue) at four UTs. TIEGCM = Thermosphere Ionosphere Electrodynamics General Circulation Model; ISR = incoherent scatter radar; UT = universal time.

The changes of solar radiation flux during the eclipse are specified by an eclipse factor function, which is calculated based on the ratio that the Sun is masked by the moon (Curto et al., 2006; Le et al., 2008). This eclipse factor function varies with longitude, latitude, and universal time. It also considers the solar extreme ultraviolet (EUV) radiation from the unmasked part of the corona. The unmasked fraction of solar EUV radiation at the totality has a minimum value of about 22%. At Millstone Hill (42.61°N, 71.48°W), the partial eclipse started at 17:27 UT, maximized at 18:46 UT with 63% obscuration, and ended at 19:59 UT. A detailed description of the solar eclipse factor calculation is given by Le et al. (2008).

We carried out two TIEGCM simulations, one with the eclipse and the other without, while all other model inputs were the same. Other than the eclipse factor function that was applied in the eclipse run, other model inputs were the observed data of $F_{10.7}$ and solar wind parameters and exactly the same for both runs. Thus, a comparison of the model results from these two runs can isolate the eclipse effect simulated by the model. The convection pattern at high latitudes was specified using the Weimer model (Weimer, 2005), driven by the observed solar wind and interplanetary magnetic field conditions. The model was run for 20 days before the eclipse day of 21 August 2017 using realistic geophysical conditions to make the modeled thermosphere and ionosphere to be in the conditions of 20 August 2017, just before the eclipse day. In this way the model results on the eclipse day would not be affected by the model's initial conditions. We then carried out model simulations for two extra days, the eclipse day and the day after, to simulate the eclipse effects and the recovery of the coupled thermosphere and ionosphere system after the eclipse. The outputs were analyzed to obtain the results presented in this paper. The time step of the simulations was 2 s.

A diagnostic analysis of the $F_2$ region ion continuity equation has been carried out to investigate the possible mechanisms responsible for the eclipse effects on the $F_2$ region and their variations. The diagnostic analysis method is described by Lei et al. (2008). Because ionospheric $F_2$ region is
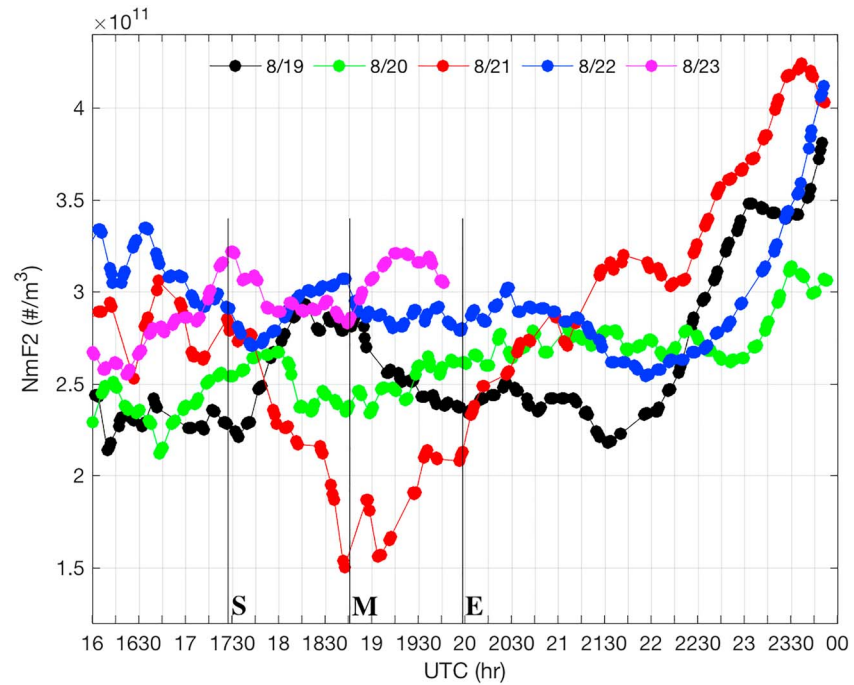
**Figure 2.** Universal time variations of $F_2$ peak electron densities observed by the Millstone Hill incoherent scatter radar from 19 to 23 August 2017. S, M, and E stand for the start, maximum, and end of the eclipse at Millstone Hill.

dominated by $O^+$, we used $O^+$ ion continuity equation to simulate electron densities in the $F_2$ region (Rishbeth & Garriott, 1969)

$$\frac{\partial N}{\partial t} = q - \beta N - \nabla \cdot \left( N \vec{V} \right) \qquad (1)$$

where $N$ is the $O^+$ or electron density, $\beta$ is the loss coefficient by molecular recombination, and $q$ is the rate of ion production. For convenience, the terms $\frac{\partial N}{\partial t}$, $q$, and $\beta N$ are referred to as $op\_dt$, $prod$, and $loss$. The transport term $-\nabla \cdot \left( N \vec{V} \right)$ is further split into transport by electric fields ($trans\_E \times B$), neutral winds ($trans\_wind$), and ambipolar diffusion ($amb\_diff$). Equation (1) is thus rewritten as

$$op\_dt = prod - loss + trans\_E \times B + trans\_wind + amb\_diff \qquad (2)$$

The top boundary condition for the $O^+$ continuity equation (1) is the $O^+$ diffusive flux. In this study, we used the method described in Chen et al. (2009, 2014) to specify this flux by using Millstone Hill observed ionospheric parameters from 19 to 23 August. This flux was also modified such that the TIEGCM simulated electron density profiles could match the observed Ne profiles (cf. Figures 1 and 3). Note that $O^+$ diffusive flux in the topside ionosphere changes greatly with geophysical conditions, such as local time, solar and geomagnetic activity, and season and magnetic latitude (Chen et al., 2009, 2010, 2014). The default TIEGCM uses a simple topside $O^+$ diffusive flux that is a constant most of the time (upward during the day and downward at night), except that it varies with local time just near dawn and dusk and with magnetic latitude at low latitudes (Wang, 1998). The direction of the model default $O^+$ diffusive flux and its values can be very different from those estimated from the radar measurements during both eclipse and noneclipse conditions. This makes the TIEGCM simulations of topside ionospheric densities with the default $O^+$ flux much smaller (by ~50% at 350 km and 21 UT) than the observations that Millstone Hill show in the late afternoon. Further observations and theoretical studies are needed to fully understand the behavior of topside $O^+$ diffusive flux and its impact on the ionosphere and are beyond the scope of the current paper.

## 3. Results and Discussion

Both observations and the model show decreases in Ne after the eclipse occurred at Millstone Hill at 17:27 UT (Figure 1). Around the eclipse period, the simulated and observed Ne in the $F_2$ region was
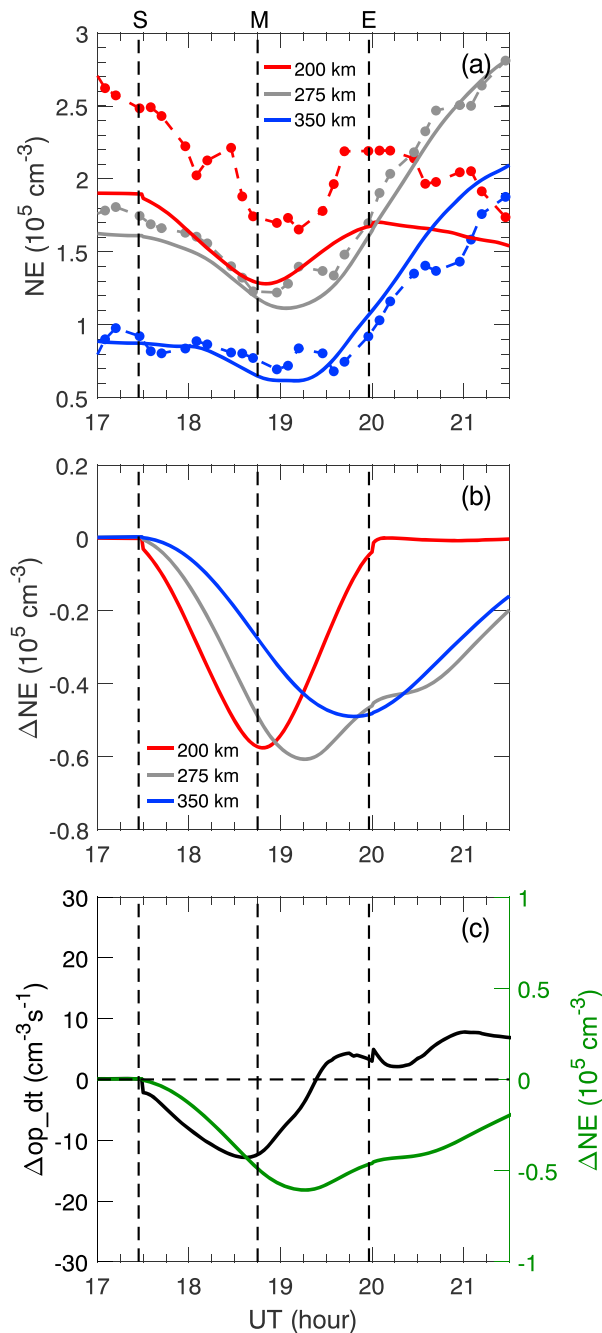
**Figure 3.** (a) Comparison of electron density between Thermosphere Ionosphere Electrodynamics General Circulation Model simulations (solid lines) and incoherent scatter radar data (dashed lines) at 200, 275, and 350 km. (b) Differential electron density from model simulations (with eclipse − without eclipse) at 200, 275, and 350 km. (c) Ne and $op\_dt$ differences at 275 km between Thermosphere Ionosphere Electrodynamics General Circulation Model simulations with and without the eclipse. UT = universal time.

comparable to or lower than that in the $F_1$ layer; thus, Ne profiles became flat (Figures 1c–1f), making it difficult and not meaningful to track the $F_2$ peak height from the observed Ne profiles.

In addition, the decrease and recovery of Ne were not symmetric relative to the temporal variation of the eclipse. The recovery of topside Ne from the maximum depletion took a longer time than the decrease of Ne before the maximum depletion in both the model and the data. Because ionosphere electron densities change with local time and solar zenith angle, the recovery of the eclipse effect in the observations is not the recovery of ionospheric electron densities back to their preeclipse values. Instead, it is the recovery back to the value that is expected if there was no eclipse. We have determined this value by comparing the values on the eclipse day with the averaged values of Ne for the three noneclipse days of 19 August, 20 August, and 22 August at the local times after the eclipse (Figures 1, 2, and 3b). The radar was turned off at about 19:45 on 08/23 UT, so no data are available after that universal time (UT). Ionospheric Ne changed throughout the day, and there was large day-to-day variability in the ionosphere, as shown in Figure 2. Figure 2 depicts the ionospheric $F_2$ peak density (Nm$F_2$) observed by the Millstone Hill radar (the plasma line measurements) around the eclipse day from 19 to 23 August 2017. Moderate geomagnetic activity occurred with a $Kp$ value of 5 before and after the eclipse day. Geomagnetic activity introduced ionospheric changes that complicated the interpretation of solar eclipse effects, especially for Millstone Hill, which is located in the subauroral zone. This makes it very difficult to establish a noneclipse reference with which a comparison can be made. On the other hand, models can more readily isolate the eclipse effects by comparing model runs with/without the eclipse.

To further illustrate the time delay between the maximum local obscuration and the maximum $F$ region electron density depletion induced by the eclipse and the asymmetric behavior of ionospheric $F_2$ region Ne during the eclipse, Figure 3a shows electron density variations at 200, 275, and 350 km from the observation (dashed lines) and model (solid lines) at Millstone Hill from 17:00 to 21:30 UT. The three vertical dashed lines indicate the beginning, maximum, and end of the partial eclipse. The modeled Ne was ~25% lower than the observations at 200 km but agreed reasonably well with the observations at higher altitudes as the topside O$^+$ flux was modified to match the observations. Both the observed and the modeled Ne were significantly larger at higher altitudes after ~20:00 UT (~15:20 LT). $F$ region electron density enhancement occurs frequently in the late afternoon at Millstone Hill in summer (Holt et al., 2002; Lee et al., 2011; Lei et al., 2005). It is not straightforward to quantify the posteclipse ionosphere recovery based on actual observations because of the day-to-day variability of the ionosphere, although the posteclipse Ne appeared to be higher than those on the other 3 days (Figure 2). The TIEGCM simulations reproduce well the evening electron density enhancements with the modified O$^+$ diffusive flux at the model top boundary. Nevertheless, further studies are needed to fully describe the role of this flux and other parameters, including neutral winds (e.g., Eccles & Burge, 1973, Lee et al., 2011, Lei et al., 2007, Zhang et al., 2012) in defining the evening behavior of the $F_2$ region ionosphere in summer.

The maximum obscuration occurred near 18:46 UT, whereas the minimum of Ne at 275 km in the model happened at about 19:15 UT (Figures 3a and 3b), a time delay of about 29 min. It is difficult to identify

the exact time delay from the data because of the large Ne fluctuations (probably traveling ionospheric disturbances, as indicated by a density increase at all heights near 19:15 UT). Nevertheless, the maximum depletion of Ne at higher altitudes (275 and 350 km) occurred at least later than 19:00 UT in the observation, which was at least 14 min later than the local maximum obscuration. This estimation is also consistent with the differential TEC keogram results in Zhang et al. (2017). The asymmetric signature of Ne is obvious in Figure 3b, which shows the differences of Ne between model runs with/with the eclipse (eclipse case-noneclipse case) at three altitudes, as the slope of Ne difference decrease from the beginning of the eclipse to the maximum depletion was different from that during the eclipse recovery and posteclipse periods. Therefore, the model was able to capture the observed ionospheric $F_2$ region electron density changes during the eclipse, including the ionospheric eclipse effects of time delay and asymmetry that we wish to study. Additionally, eclipse effects cannot be easily isolated from the observations as the ionosphere varies with changing geophysical conditions.

In the rest of the paper, we will examine the differences between model runs with and without eclipse to delineate the eclipse effects as model captures reasonably well the observed ionospheric $F_2$ region electron density variations caused by the eclipse. We will determine the physical processes driving these effects and their temporal and spatial variations through diagnostic analysis of the model outputs. We will primarily focus on the $F_2$ region eclipse effects where winds, ambipolar diffusion, and electric fields play significant roles, whereas the eclipse effects in the $E$ and $F_1$ regions are mainly controlled by fast photochemistry and well understood (e.g., Adeniyi et al., 2009, Rishbeth, 1968).

Figure 3b shows Ne differences at 200, 275, and 350 km between model runs with/without the eclipse (with eclipse − without eclipse). Ne at 200 km attained a minimum at the maximum obscuration and recovered at the end of the eclipse. Ne at higher altitudes in the $F_2$ region approached maximum depletion at a later time. The time delays for the modeled Ne at 275 and 350 km were about 29 and 60 min, respectively. Figure 3b also shows that at altitudes above ~200 km, $F_2$ region electron densities were slow to recover to the values of the model run without the eclipse. The cause of this time delay and its asymmetric characteristic (fast decrease and slow recovery) of ionospheric $F_2$ region Ne variations is that the physical processes determining $F_2$ region electron densities change over the course of the eclipse. In the later part of this section, we will delineate in detail these processes and their dynamic changes during and after the eclipse.

Figure 3c again shows differential Ne at 275 km (green line), along with the difference of total $O^+$ change with time ($\Delta op\_dt$, black line), between model runs with/without the eclipse. $\Delta op\_dt$ was negative from the beginning of the eclipse and approached a minimum near the maximum obscuration, it then became less negative with smaller absolute values as the moon shadow waned, when solar radiation was still weaker than that in the noneclipse case. The difference in the rate of $O^+$ change ($\Delta op\_dt$) after the maximum obscuration was negative until ~19:15 UT (green line); thus, electron densities were continuously decreasing and attained a minimum at 275 km when $\Delta op\_dt$ became zero near 19:15 UT. From ~19:15 UT, $\Delta op\_dt$ became positive with a value of about 4–5 cm$^{-3}$/s until the end of the eclipse and remained positive after that. The $\Delta op\_dt$ increase after ~19:15 UT was smaller than $\Delta op\_dt$ before and around the maximum local obscuration. Thus, at 275-km height, Ne was continuously increased after ~19:15 UT but at a relatively slow and steady rate. This led to slow recovery of Ne in the later part of the eclipse recovery phase between ~19:15 and ~20:00 UT and in the posteclipse period after 20:00 UT. For instance, from the beginning of the eclipse at 17:27 to 19:15 UT, in a time interval of 108 min, the difference of Ne changed from 0.0 to about $-0.6 \times 10^5$ cm$^{-3}$, whereas after the eclipse from 19:25 to 21:15 UT, in roughly the same time interval (120 min), the Ne difference was still negative, and about $-0.25 \times 10^5$ cm$^{-3}$, did not return to zero. Therefore, while solar radiation change should be almost symmetric about the local maximum obscuration, the response of the ionosphere is not because other processes, including neutral composition, ambipolar diffusion, and transport by winds and electric fields, play a significant role in controlling the ionospheric $F_2$ region response to the eclipse.

Figure 4 gives the differences in electron densities (Figure 4a, in unit of per cubic centimeter) and the terms (time rate of change of $O^+$) in the ion continuity equation (2) (Figures 4b–4f, in unit of per cubic centimeter per second) between model runs with and without eclipse effects. The differences seen in the figure are thus the eclipse effects on each parameter and the process it represents (cf. equation (2)). For simplicity, hereafter we will just refer to the names of these parameters, but they actually represent the differences of the results between eclipse and noneclipse runs. For instance, a negative value or depletion in Figure 4a indicates that
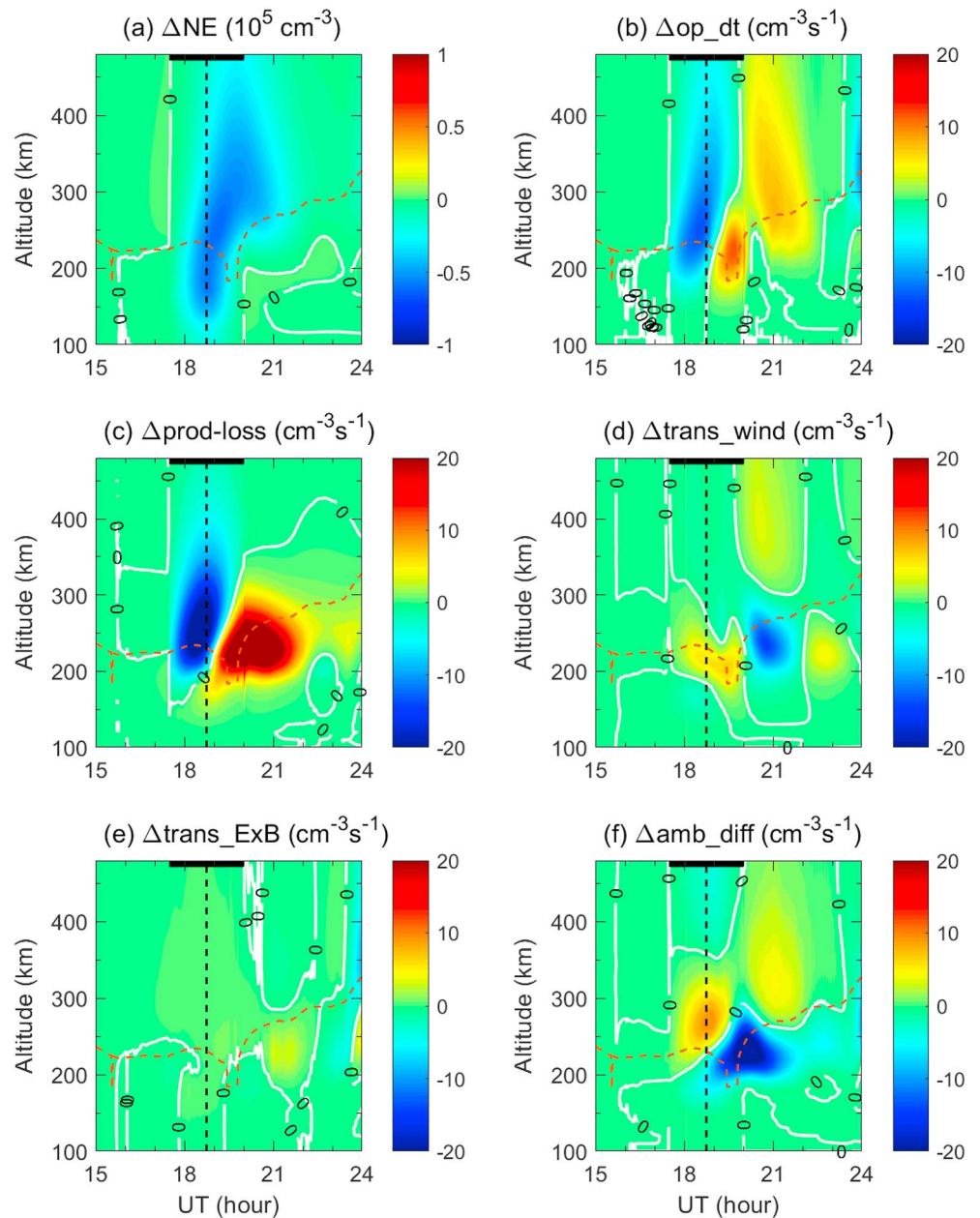
**Figure 4.** UT and altitudinal variations of differential (a) electron density (in unit of $10^5 \, cm^{-3}$) and (b–f) terms (in unit of per cubic centimeter per second) between the Thermosphere Ionosphere Electrodynamics General Circulation Model simulations with and without the eclipse (with eclipse − without eclipse). The terms shown are (b) *op_dt*, (c) *prod-loss*, (d) *trans_wind*, (e) *trans_ExB*, and (f) *amb_diff*, respectively. The vertical dashed lines show the time of maximum obscuration at Millstone Hill, while the black bars stand for the duration of the partial eclipse. The red dashed lines are the $F_2$ region peak height. UT = universal time.

the TIEGCM simulated electron densities in the eclipse case are smaller than those in the noneclipse one and thus represents the case that the eclipse depletes the ionospheric electron densities. In Figure 4, a time integration of $\Delta op\_dt$ (Figure 4b), to say 21 UT, gives the Ne difference ($\Delta Ne$) in Figure 4a at 21 UT. The sum of all the terms in Figures 4c–4f at a particular UT gives the value of $\Delta op\_dt$ in Figure 4b at that UT. Note that Figure 4 is in the height coordinates. We choose height since the observations are in height coordinates. We also plot Figure 4 in pressure level coordinates (not shown). The results are similar and consistent. The red dashed lines show the $F_2$ peak height. Electron densities decreased immediately after the onset of the partial eclipse at 17:27 UT at all heights. However, at the maximum obscuration

(18:46 UT) the largest decrease occurred below about 200 km where ionospheric electron densities were mostly controlled by photochemistry. The maximum electron density decrease, however, occurred at about 19:15 UT at ~275 km: this is a time delay of about 29 min. The delay time was longer at higher altitudes. Above ~180 km in the $F_2$ region, the depletion of electron densities closely followed the temporal variation of $O^+$ change ($\Delta op\_dt$; Figure 4b). The maximum Ne depletion occurred when $\Delta op\_dt$ was zero near 275 km. Below about the $F_2$ peak height, there was a period of a large positive $\Delta op\_dt$ from about 19 to 20 UT, which led to the rapid recovery of Ne.

Figure 4c shows the difference in $O^+$ rate of changes related to chemical process, that is, the combined effect of $O^+$ production due to solar EUV photoionization and loss by molecular recombination. Comparing Figures 4b and 4c, we can see that the temporal changes of $O^+$ were different from those of the chemical production and loss rate. For instance, before the vertical line of maximum local obscuration at 18:46 UT, ion production rate was significantly reduced between ~200 and 300 km due to the eclipse effect (Figure 4c), but the total $O^+$ change rate (Figure 4b) was not as large as that in Figure 4c. Furthermore, ion production rate was large ($>20$ cm$^{-3}$/s) just below the $F_2$ peak and above 200 km after 19:00 UT, but the $\Delta op\_dt$ term in Figure 4b in the same time interval and altitude range did not show such a large $O^+$ change rate (with a magnitude of ~10 cm$^{-3}$/s), indicating that other processes contributed significantly to the eclipse-induced variation of $F_2$ region plasma density throughout the eclipse. For instance, Ne changes induced by wind transport below the $F_2$ peak and ambipolar diffusion near the maximum obscuration were positive with a magnitude of about 5–10 cm$^{-3}$/s and thus balanced out partially the large decrease of $O^+$ production rate.

In Figure 4c, the $\Delta prod\text{-}loss$ term was negative from about 180 km in the early phase of the eclipse, which was the result of the loss of EUV radiation due to the eclipse. However, shortly after the maximum obscuration, the $\Delta prod\text{-}loss$ term became positive from ~180 km to an altitude of 300 km (above the $F_2$ peak). Note here that $\Delta prod\text{-}loss$ in Figure 4c is the difference between cases with/without the eclipse. Thus, the large positive $\Delta prod\text{-}loss$ values after the maximum obscuration were not caused by the recovery of solar EUV but a thermospheric composition effect, as solar EUV radiation was still low at that time as the site was still in the moon shadow. Due to the decreased neutral temperature in the eclipse zone, winds were convergent toward the center of the moon shadow (cf. Figure 6), causing downwelling and leading to an increased $O/N_2$ ratio (e.g., Burns, Killeen, Carignan, & Roble, 1995; Burns, Killeen, Deng, et al., 1995). The increase in $O/N_2$ evidently overcame the effect of the reduced solar EUV radiation and caused an increased $O^+$ production rate. $O^+$ production became smaller after about 22 UT as $O/N_2$ recovered toward the noneclipse case.

The contribution of electric-field-induced plasma drifts to eclipse-induced $F_2$ region density changes was minor during the eclipse but became relatively large just below the $F_2$ peak after about 21:00 UT (Figure 4e). The magnitude of $O^+$ rate of change by ambipolar diffusion was about 5 cm$^{-3}$/s. The cause of the changes in electric fields was eclipse-induced disturbance winds. The eclipse-induced effects of electric fields on ionospheric density changes at middle latitudes are smaller compared with those at low and equatorial latitudes, where electric fields can be a dominant process driving the changes in $F_2$ region electron densities during eclipses (Chen et al., 2011, 2015; Madhav Haridas & Manju, 2012; Shweta Sharma et al., 2010).

The eclipse effects of wind transport are shown in Figure 4d. Around the local maximum obscuration, the wind contribution to Ne changes between about 180 and 250 km, just below the $F_2$ peak height, was positive, indicating that winds transported plasma into this altitude region. Near 20:00 UT the meridional wind direction changed from northward to southward (cf. Figure 6). The altitude profiles of the contribution of winds to plasma density variations also changed. In Figure 4d we can see that before 20:00 UT the winds acted to increase the electron densities at and below the $F_2$ peak with a rate of electron density change of ~5 cm$^{-3}$/s, whereas after 20:00 UT the effects of winds were to decrease the electron densities from about 200 to 250 km and to increase the densities above about 300 km. For instance, the rate of electron density decreases caused by the winds was close to $-15$ cm$^{-3}$/s at 21:00 UT just below the $F$ peak at about 220 km. Note that the winds cannot directly produce nor destroy plasma but transport it. Thus, the positive values of the contribution to $O^+$ change in the topside ionosphere show that the winds transported plasma from lower altitudes to higher altitudes and thus increased the topside ionospheric plasma density, whereas the negative values in the lower $F_2$ region indicate that winds transported the plasma from the region to the topside and thus depleted lower $F_2$ region electron densities. Below the $F_2$ peak vertical gradients of electron density increase with

altitude, an upward transport effect along the magnetic field lines by meridional winds thus depletes the bottomside electron density. Above the $F_2$ peak vertical gradients of electron density decrease with altitude, so the same upward transport by winds increases topside electron density.

The winds transported the plasma into the topside ionosphere but depleted Ne in the lower $F_2$ region after about 20:00 UT (Figure 4d). Since plasma can only be transported by ion-neutral collision along the filed lines, winds in the geographic coordinates have to be projected first onto the magnetic meridional plane using $-U_n \sin D + V_n \cos D$, where $U_n$ and $V_n$ are zonal and meridional winds. The contribution of winds to plasma transport at Millstone Hill is mostly, but definitely not only, from the meridional winds, as the declination angle $D$ there is $-13°$. The plasma transport by winds was thus mainly caused by the meridional winds $V_n$. Figure 6d shows that near Millstone Hill at 20:35 UT the meridional winds were southward and thus pushed the plasma upward along the field lines.

Ambipolar diffusion (Figure 4f) also plays a significant role in changing $F_2$ region electron densities at middle latitudes during the eclipses (e.g., Chukwuma & Adekoya, 2016). The effects of ambipolar diffusion were positive above the $F_2$ peak and negative below near the maximum obscuration. From about 19:00 to 21:00 UT and just below the $F_2$ peak, ambipolar diffusion was strongly negative and tended to balance out the net increase in electron density caused by the photochemical effect (photoionization and recombination loss; Figure 4c). Note that ambipolar diffusion is a reactive action to the changes in plasma pressure along magnetic field lines that have been produced by other processes. Eclipse-induced electron temperature depletion maximized at about 220 km near 18:40 UT (not shown). The reduced electron temperature and electron density caused low plasma pressure in the region to lead to a large plasma pressure gradient that drove the plasma into the region and thereby contributed to the modification of the overall vertical profile of $\Delta op\_dt$.

After ~21:00 UT and in the topside ionosphere above the $F_2$ peak, ambipolar diffusion was positive, acted to increase the electron densities. The magnitude of electron density change caused by ambipolar diffusion at ~300 km and 21 UT was ~5 cm$^{-3}$/s. Therefore, after the eclipse maximum, ambipolar diffusion moves the plasma from below the $F_2$ peak to the topside, relative to the noneclipse case. The electron density change in the topside ionosphere due to transport by winds at the same time was also positive with a relatively small magnitude (Figure 4d). Thus, Figure 4 shows that the recovery of the topside ionosphere was primarily controlled by the refilling of plasma due to winds and ambipolar diffusion. The contribution from the chemical effect in the topside was minor. As shown in Figure 3c, the rate of change of Ne at 275 km ($\Delta op\_dt$, black line) was in the range of 3–7 cm$^{-3}$/s after 19:15 UT. This was smaller than the rate of change of Ne before 19:15 UT and led to slow recovery of the topside ionosphere after the eclipse (green line in Figure 3c).

Thus, the changes of plasma density caused by transport due to eclipsed-induced wind variations (Figure 4d), chemical production and loss (Figure 4c), and ambipolar diffusion (Figure 4f) produced a vertical profile of $\Delta op\_dt$ (Figure 4b) that resulted in the temporal and spatial variations of $F_2$ region Ne shown in Figure 4a during and after the eclipse.

To illustrate more clearly the relative contribution of each term in equation (2) to the eclipse-induced changes of ionospheric electron densities and its temporal variation, we show in Figure 5 the differences between electron densities and differences in the rates of change of O$^+$ terms in the ion continuity equation (2) between model runs with and without eclipse effects at 200, 275, and 350 km. The change of Ne caused by the eclipse at a particular UT is the time integration of the total rate of O$^+$ change ($\Delta op\_dt$, black lines) in Figures 5b–5d, which is the sum of the other terms shown in the respective figures. Therefore, at 200 km (Figure 5b), Ne decreased from the beginning of the eclipse until about the maximum obscuration time when it reached a minimum value of about $-0.5 \times 10^5$ cm$^{-3}$. After that time $\Delta op\_dt$ (black line) became zero and positive so Ne began to recover. Ambipolar diffusion (green line) acted always to reduce Ne at this altitude; its magnitude increased with time until about 20:00 UT and then decreased toward zero values. The wind transport effects were to increase Ne at the altitude during the eclipse but to decrease it shortly after the eclipse. We can also see that the $\Delta prod\text{-}loss$ term was first negative until the maximum obscuration time; it then became strongly positive to increase Ne after the maximum obscuration time. As explained earlier, this positive $\Delta prod\text{-}loss$ was primarily due to the thermospheric composition effect. Note that $\Delta op\_dt$ became about zero near the end of the eclipse and the ionosphere recovered (solid line in Figure 5a); however, the
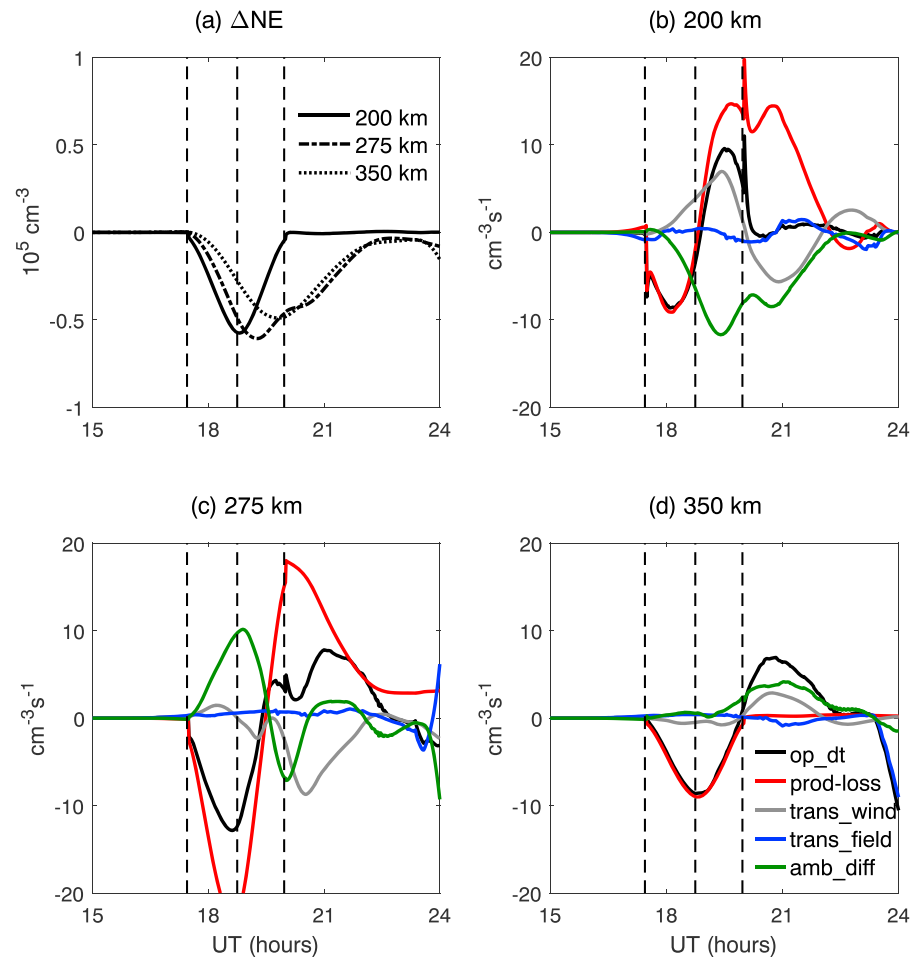
**Figure 5.** (a) UT variations of differential electron density (in unit of $10^5$ cm$^{-3}$) between the Thermosphere Ionosphere Electrodynamics General Circulation Model simulations with and without the eclipse (with eclipse − without eclipse). (b–f) Differences of O$^+$ rate of change terms (in unit of per cubic centimeter per second) between the Thermosphere Ionosphere Electrodynamics General Circulation Model simulations with and without the eclipse (with eclipse − without eclipse) at 200, 275, and 375 km, respectively. The vertical dashed lines show the time of beginning, maximum obscuration, and end of the eclipse at Millstone Hill. UT = universal time.

terms were not recovered at all. They just balanced out such that the electron densities in the eclipse case and noneclipse case were about the same.

Similar analysis can also be made for the cases at 275 and 350 km, but we will not go in detail. One striking feature worth noting here is that at 350 km in the topside ionosphere (Figure 5d), Ne decreases were mainly caused by the negative values of the *prod-loss* term or eclipse-induced ionization loss. However, after the eclipse the *op_dt* term (black line) consisted of mainly the wind and ambipolar diffusion terms, indicating that they were the primary processes that drive the recovery of the eclipse effects in the topside ionosphere.

To better understand the effects of neutral wind changes on the transport of ionospheric plasma and Ne variations, we show the differences in neutral temperature (K) and neutral winds (m/s, vector) between the TIEGCM runs with and without the eclipse at four UTs in Figure 6. The red dot illustrates the location of Millstone Hill, and the white cross gives the position of eclipse totality at the corresponding UT. For all UTs, the difference winds were directed toward the lowest temperature region, but their convergence point occurred at a later local time. This is related to the fact that wind velocity changes are the cumulative effect of forcing (acceleration) over time. The speed and direction of winds do not necessarily correspond to the instant forcing pattern at a particular time. Furthermore, the winds also depend on other forcing processes, such as ion drag and the Coriolis force; thus, the wind pattern is not fully aligned with the temperature
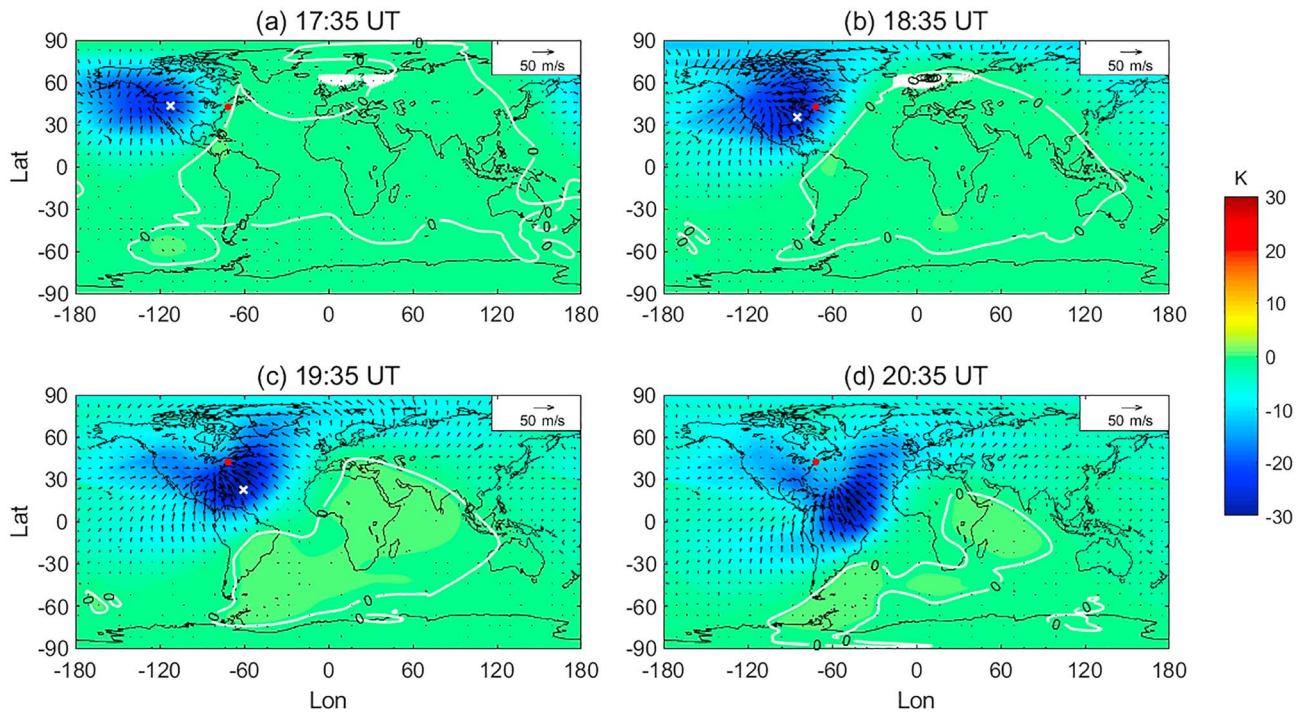
**Figure 6.** A global view of the changes of neutral temperature (color contours, in unit of Kelvin) and winds (vector arrows, in unit of meter per second) differences between Thermosphere Ionosphere Electrodynamics General Circulation Model simulations with/without the eclipse at four universal times during the eclipse on 21 August 2017. The red dot indicates the location of Millstone Hill, and white cross gives the location of eclipse totality for the corresponding universal time.

structure that produces the pressure gradient force. Nevertheless, the difference wind pattern was correlated well with the eclipse-induced temperature difference pattern. Therefore, the difference winds were northwestward at Millstone Hill before the maximum obscuration at Millstone Hill as the wind convergence center was located west and north to the radar site (Figures 6a and 6b). The difference winds then changed to southeastward (Figures 6c and 6d) after the maximum obscuration and in the posteclipse phase, as the location of temperature minimum and wind convergence center moved to the southeast of Millstone Hill.

The effects of wind changes on the ionosphere are mostly determined by the meridional wind direction, when the changes in meridional and zonal winds are of the similar magnitude. The magnetic declination angle ($D$) at Millstone Hill is $-13°$. Thus, from the projection of wind velocity along the magnetic field lines, $-U_n \sin D + V_n \cos D$, we can see that, when $D$ is small, the contribution of winds to plasma transport is primarily from the meridional winds. Before about 20:00 UT, the difference winds were northward at the radar site, pushing the plasma downward along field lines; thus, the wind transport effect was negative above the $F_2$ peak and positive below the peak (Figure 4d). After about 20:00 UT, the difference winds were southward, pushing the plasma upward. The contribution of the difference winds to eclipsed-induced ionospheric $F_2$ region density changes from this time onward was therefore positive above the $F_2$ peak and negative below. Figures 4d and 6 demonstrate that eclipse-induced wind changes can contribute significantly to the changes in ionospheric $F_2$ region electron densities. This contribution is mostly from the meridional winds. The magnitude and temporal variations of the wind contribution depend on the relative locations of the observation site and the site of the eclipse totality.

Finally, it should be noted that the eclipse effects are local time and altitude dependent and the relative contributions of the physical processes to these effects are also local time and altitude dependent. For instance, between the beginning of the eclipse and the local maximum obscuration, reduced photoionization and wind transport dominated the change of $F_2$ region electron density below the $F_2$ peak, whereas the reduced photoionization and changed ambipolar diffusion caused the largest variations above the $F_2$ peak. On the other hand, after about 20:00 UT, changes in ambipolar diffusion (Figure 4f) and O$^+$ production

(Figure 4c) were the major contributors to the changes of electron densities in the lower $F_2$ region, with some contribution from the winds (Figure 4d) and transport by electric fields (Figure 4e), but at the same time, in the topside ionosphere above 350 km, the dominant processes were ambipolar diffusion and wind transport, with little contribution from the chemical production or loss process. Thus, the results shown in this paper for an afternoon partial eclipse at middle latitudes may not be the same as those for the eclipse occurring at other times and latitudes or with a different kind of eclipses (e.g., Chen et al., 2011, 2015; Madhav Haridas & Manju, 2012; Shweta Sharma et al., 2010).

## 4. Summary

In this paper, we presented middle-latitude ionospheric $F_2$ region density variations observed by the ISR at Millstone Hill where a partial solar eclipse occurred on 21 August 2017. A high-resolution, first-principles self-consistent model of the coupled thermosphere-ionosphere system was used to simulate the observed eclipse effects. The effects are evidently very dynamic and involve in multiple chemical and physical processes that have their own spatial and temporal variations with the eclipse. By diagnostically and quantitatively analyzing the model outputs, we delineated the physical processes that drive the observed and modeled changes of $F_2$ region electron density during the partial eclipse. Specifically, the main findings of the present work are as follows:

1. Both the observations and model simulations show that there is a time delay between the largest eclipsed-induced $F_2$ region electron density depletion and the local maximum obscuration. The time delay increases with altitude. It is also found that the recovery of the $F_2$ region eclipse effect is a slow process, compared to the decrease of $F_2$ region electron density from the beginning of the eclipse to the time of maximum obscuration.
2. As the moon shadow enters, maximizes, and leaves a particular observation site, the disturbance winds change direction and their effects on the $F_2$ region electron densities also vary, from pushing the plasma downward before the local maximum obscuration to transporting it upward to the topside ionosphere after the local maximum obscuration.
3. The low temperature and convergence of disturbance winds in the moon shadow also cause local enhancement of $O/N_2$ shortly after the local maximum obscuration, leading to a large ion production rate and contributing significantly to the recovery of the ionosphere near and below the $F_2$ peak. This work, therefore, highlights the significant effects of eclipse-induced thermospheric changes on the overall ionosphere behavior during and after the eclipse.
4. Ambipolar diffusion also contributes greatly to the eclipsed-induced Ne changes. Ambipolar diffusion reacts to plasma density and temperature variations induced by changes in electric fields, winds, and composition, as well as direct EUV ionization and heating. It first transports plasma into the $F$ region from the beginning of the eclipse until the local maximum obscuration. It then moves the plasma upward from below the $F_2$ peak to the topside due to the production of more ions in the lower $F_2$ region after the local maximum obscuration of the eclipse.
5. The winds, composition, and ambipolar diffusion show different temporal and vertical changes during the eclipse; their combined effects determine the temporal and spatial variability of the eclipse effects on the $F_2$ region electron density at middle latitudes during and after the eclipse.
6. The recovery and the variation of the topside ionosphere electron density after the eclipse are mostly determined by the refilling by winds and ambipolar diffusion. Both winds and ambipolar diffusion transport plasma upward to higher altitudes from the lower $F_2$ region where more ions are produced after the eclipse.
7. A combination of solar radiation change and the temporal and spatial variations of the above-mentioned processes could explain the time delay and asymmetric characteristic (fast decrease and slow recovery) of the response of topside ionospheric $F_2$ region electron density to the eclipse seen in Millstone Hill ISR observations.

In this study, we provide, through term analysis, a quantitative and complete picture of the roles of eclipse-induced disturbance winds, thermospheric composition changes, ambipolar diffusion, and electric fields in determining the response of the ionospheric $F_2$ region to a partial eclipse at middle latitudes and the temporal and spatial variation of this response. We showed that the relative contribution of each process to

the eclipse effects varies with time and altitude during and after the eclipse. In the future, both global observations of neutral and ionospheric parameters and advanced first principles modeling are required to fully understand how these processes vary dynamically and interact nonlinearly with each other to determine the behavior of the coupled thermosphere-ionosphere system during transient geophysical conditions, such as the eclipse occurring at various times and latitudes.

# References

Adekoya, B. J., & Chukwuma, V. U. (2016). Ionospheric $F_2$ layer responses to total solar eclipses at low and mid-latitude. *Journal of Atmospheric and Solar-Terrestrial Physics*, *138-139*, 136–160. https://doi.org/10.1016/j.jastp.2016.01.006

Adeniyi, J. O., Oladipo, O. A., Radicella, S. M., Adimula, I. A., & Olawepo, A. O. (2009). Analysis on 29 March 2006 eclipse effect on the ionosphere over Ilorin, Nigeria. *Journal of Geophysical Research*, *114*, A11303. https://doi.org/10.1029/2009JA014416

Afraimovich, E. L., Kosogorov, E. A., & Lesyuta, O. S. (2002). Effects of the August 11, 1999 total solar eclipse as deduced from total electron content measurements at the GPS network. *Journal of Atmospheric and Solar-Terrestrial Physics*, *64*(18), 1933–1941. https://doi.org/10.1016/S1364-6826(02)00221-3

Afraimovich, E. L., Palamartchouk, K. S., Perevalova, N. P., Chernukhov, V. V., Lukhnev, A. V., & Zalutsky, V. T. (1998). Ionospheric effects of the solar eclipse of March 9, 1997, as deduced from GPS data. *Geophysical Research Letters*, *25*(4), 465–468. https://doi.org/10.1029/98GL00186

Afraimovich, E. L., Voeykov, S. V., Perevalova, N. P., Vodyannikov, V. V., Gordienko, G. I., Litvinov, Y. G., & Yakovets, A. F. (2007). Ionospheric effects of the March 29, 2006, solar eclipse over Kazakhstan. *Geomagnetism and Aeronomy*, *47*(4), 461–469. https://doi.org/10.1134/S0016793207040068

Baron, M. J., & Hunsucker, R. D. (1973). Incoherent scatter radar observations of the auroral zone ionosphere during the total solar eclipse of July10, 1972. *Journal of Geophysical Research*, *78*(31), 7451–7460. https://doi.org/10.1029/JA078i031p07451

Boitman, O. N., Kalikhman, A. D., & Tashchilin, A. V. (1999). The midlatitude ionosphere during the total solar eclipse of March 9, 1997. *Journal of Geophysical Research*, *104*(A12), 28,197–28,206. https://doi.org/10.1029/1999JA900228

Burmaka, V. P., & Chernogor, L. F. (2013). Solar eclipse of August 1, 2008, above Kharkov: 2. Observation results of wave disturbances in the ionosphere. *Geomagnetism and Aeronomy*, *53*(4), 479–491. https://doi.org/10.1134/S0016793321304004X

Burns, A. G., Killeen, T. L., Carignan, G. R., & Roble, R. G. (1995). Large enhancements in the O/N2 ratio in the evening sector of the winter hemisphere during geomagnetic storms. *Journal of Geophysical Research*, *100*(A8), 14,661–14,671. https://doi.org/10.1029/94JA03235

Burns, A. G., Killeen, T. L., Deng, W., Carignan, G. R., & Roble, R. G. (1995). Geomagnetic storm effects in the low- to middle-latitude upper thermosphere. *Journal of Geophysical Research*, *100*(A8), 14,673–14,691. https://doi.org/10.1029/94JA03232

Chen, G., Wu, C., Huang, X., Zhao, Z., Zhong, D., Qi, H., et al. (2015). Plasma flux and gravity waves in the midlatitude ionosphere during the solar eclipse of 20 May 2012. *Journal of Geophysical Research: Space Physics*, *120*, 3009–3020. https://doi.org/10.1002/2014JA020849

Chen, G., Zhao, Z., Ning, B., Deng, Z., Yang, G., Zhou, C., et al. (2011). Latitudinal dependence of the ionospheric response to solar eclipse of 15 January 2010. *Journal of Geophysical Research*, *116*, A06301. https://doi.org/10.1029/2010JA016305

Chen, G.-M., Xu, J., Wang, W., Lei, J., & Deng, Y. (2009). Field-aligned plasma diffusive fluxes in the topside ionosphere from radio occultation measurements of CHAMP. *Journal of Atmospheric and Solar - Terrestrial Physics*, *71*(8-9), 967–974. https://doi.org/10.1016/j.jastp.2009.03.027

Chen, G.-M., Xu, J., Wang, W., Lei, J., & Deng, Y. (2010). Plasma diffusive flows in the topside ionosphere from radio occultation measurements by COSMIC. *Chinese Journal of Space Science*, *30*, 121–131.

Chen, G.-M., Xu, J., Wang, W., Lei, J., & Zhang, S.-R. (2014). The responses of ionospheric topside diffusive fluxes to two geomagnetic storms in October 2002. *Journal of Geophysical Research: Space Physics*, *119*, 6806–6820. https://doi.org/10.1002/2014JA020013

Cherniak, I., & Zakharenkova, I. (2018). Ionospheric total electron content response to the great American solar eclipse of 21 August 2017. *Geophysical Research Letters*, *45*, 1199–1208. https://doi.org/10.1002/2017GL075989

Chukwuma, V. U., & Adekoya, B. J. (2016). The effects of March 20 2015 solar eclipse on the $F_2$ layer in the mid-latitude. *Advances in Space Research*, *58*(9), 1720–1731. https://doi.org/10.1016/j.asr.2016.06.038

Coster, A. J., Goncharenko, L., Zhang, S.-R., Erickson, P. J., Rideout, W., & Vierinen, J. (2017). GNSS observations of ionospheric variations during the 21 August 2017 solar eclipse. *Geophysical Research Letters*, *44*, 12,041–12,048. https://doi.org/10.1002/2017GL075774

Curto, J. J., Heilig, B., & Piñol, M. (2006). Modeling the geomagnetic effects caused by the solar eclipse of 11 August 1999. *Journal of Geophysical Research*, *111*, A07312. https://doi.org/10.1029/2005JA011499

Dang, T., Lei, J., Wang, W., Burns, A., Zhang, B., & Zhang, S.-R. (2018). Suppression of the polar tongue of ionization during the 21 August 2017 solar eclipse. *Geophysical Research Letters*, *45*(7), 2918–2925. https://doi.org/10.1002/2018GL077328

Dang, T., Lei, J., Wang, W., Zhang, B., Burns, A., le, H., et al. (2018). Global responses of the coupled thermosphere and ionosphere system to the August 2017 Great American Solar Eclipse. *Journal of Geophysical Research: Space Physics*, *123*, 7040–7050. https://doi.org/10.1029/2018JA025566

Ding, F., Wan, W., Ning, B., Liu, L., Le, H., Xu, G., et al. (2010). GPS TEC response to the 22 July 2009 total solar eclipse in East Asia. *Journal of Geophysical Research*, *115*, A07308. https://doi.org/10.1029/2009JA015113

Domnin, I. F., Yemel'yanov, L. Y., Kotov, D. V., Lyashenko, M. V., & Chernogor, L. F. (2013). Solar eclipse of August 1, 2008, above Kharkov: 1. Results of incoherent scatter observations. *Geomagnetism and Aeronomy*, *53*(1), 113–123. https://doi.org/10.1134/S0016793213010076

Eccles, D., & Burge, J. D. (1973). The behaviour of the upper ionosphere over North America at sunset. *Journal of Atmospheric and Terrestrial Physics*, *35*(11), 1927–1934. https://doi.org/10.1016/0021-9169(73)90110-4

Evans, J. V. (1965a). An $F$ region eclipse. *Journal of Geophysical Research*, *70*(1), 131–142. https://doi.org/10.1029/JZ070i001p00131

Evans, J. V. (1965b). On the behavior of foF2 during solar eclipses. *Journal of Geophysical Research*, *70*(3), 733–738. https://doi.org/10.1029/JZ070i003p00733

Farges, T., Jodogne, J. C., Bamford, R., Le Roux, Y., Gauthier, F., Vila, P. M., et al. (2001). Disturbances of the western European ionosphere during the total solar eclipse of 11 August 1999 measured by a wide ionosonde and radar network. *Journal of Atmospheric and Solar-Terrestrial Physics*, *63*(9), 915–924. https://doi.org/10.1016/S1364-6826(00)00195-4

Grigorenko, E. I., Lyashenko, M. V., & Chernogor, L. F. (2008). Effects of the solar eclipse of March 29, 2006, in the ionosphere and atmosphere. *Geomagnetism and Aeronomy*, *48*(3), 337–351. https://doi.org/10.1134/S0016793208030092

Holt, J. M., Zhang, S.-R., & Buonsanto, M. J. (2002). Regional and local ionospheric models based on Millstone Hill incoherent scatter radar data. *Geophysical Research Letters*, *29*(8), 1207. https://doi.org/10.1029/2002GL014678

Huba, J. D., & Drob, D. (2017). SAMI3 prediction of the impact of the 21 August 2017 total solar eclipse on the ionosphere/plasmasphere system. *Geophysical Research Letters*, *44*, 5928–5935. https://doi.org/10.1002/2017GL073549

Korenkov, Y. N., Klimenko, V. V., Bessarab, F. S., Nutsvalyan, N. S., & Stanislawska, I. (2003). Model/data comparison of the $F_2$-region parameters for the 11 August 1999 solar eclipse. *Advances in Space Research*, *31*(4), 995–1000. https://doi.org/10.1016/S0273-1177(02)00816-5

Kurkin, V. I., Nosov, V. E., Potekhin, A. P., Smirnov, V. F., & Zherebtsov, G. A. (2001). The March 9, 1997 solar eclipse ionospheric effects over the Russian Asian region. *Advances in Space Research*, *27*(8), 1437–1440. https://doi.org/10.1016/S0273-1177(01)00030-8

Le, H., Liu, L., Yue, X., & Wan, W. (2008). The midlatitude $F_2$ layer during solar eclipses: Observations and modeling. *Journal of Geophysical Research*, *113*, A08309. https://doi.org/10.1029/2007JA013012

Le, H., Liu, L., Yue, X., Wan, W., & Ning, B. (2009). Latitudinal dependence of the ionospheric response to solar eclipses. *Journal of Geophysical Research*, *114*, A07308. https://doi.org/10.1029/2009JA014072

Le, H., et al. (2010). Observations and modeling of the ionospheric behaviors over the east Asia zone during the 22 July 2009 solar eclipse. *Journal of Geophysical Research*, *115*, A10313. https://doi.org/10.1029/2010JA015609

Ledig, P. G., Jones, M. W., Giesecke, A. A., & Chernosky, E. J. (1946). Effects on the ionosphere at Huancayo, Peru, of the solar eclipse, January 25, 1944. *Journal of Geophysical Research*, *51*(3), 411–418. https://doi.org/10.1029/TE051i003p00411

Lee, W. K., Kil, H., Kwak, Y.-S., Wu, Q., Cho, S., & Park, J. U. (2011). The winter anomaly in the middle-latitude F region during the solar minimum period observed by the constellation observing system for meteorology, ionosphere, and climate. *Journal of Geophysical Research*, *116*, A02302. https://doi.org/10.1029/2010JA015815

Lei, J., Liu, L., Wan, W., & Zhang, S.-R. (2005). Variations of electron density based on long-term incoherent scatter radar and ionosonde measurements over Millstone Hill. *Radio Science*, *40*, RS2008. https://doi.org/10.1029/2004RS003106

Lei, J., Roble, R. G., Kawamura, S., & Fukao, S. (2007). A simulation study of thermospheric neutral winds over the MU radar. *Journal of Geophysical Research*, *112*, A04303. https://doi.org/10.1029/2006JA012038

Lei, J., Wang, W., Burns, A. G., Solomon, S. C., Richmond, A. D., Wiltberger, M., et al. (2008). Observations and simulations of the ionospheric and thermospheric response to the December 2006 geomagnetic storm: Initial phase. *Journal of Geophysical Research*, *113*, A01314. https://doi.org/10.1029/2007JA012807

Lyashenko, M. V., & Chernogor, L. F. (2013). Solar eclipse of August 1, 2008, over Kharkov: 3. Calculation results and discussion. *Geomagnetism and Aeronomy*, *53*(3), 367–376. https://doi.org/10.1134/S0016793213020096

Madhav Haridas, M. K., & Manju, G. (2012). On the response of the ionospheric F region over Indian low-latitude station Gadanki to the annular solar eclipse of 15 January 2010. *Journal of Geophysical Research*, *117*, A01302. https://doi.org/10.1029/2011JA016695

Müller-Wodarg, I. C. F., Aylward, A. D., & Lockwood, M. (1998). Effects of a mid-latitude solar eclipse on the thermosphere and ionosphere—A modelling study. *Geophysical Research Letters*, *25*(20), 3787–3790. https://doi.org/10.1029/1998GL900045

Picone, J. M., Hedin, A. E., Drob, D. P., & Aikin, A. C. (2002). NRLMSISE-00 empirical model of the atmosphere: Statistical comparisons and scientific issues. *Journal of Geophysical Research*, *107*(A12), 1468. https://doi.org/10.1029/2002JA009430

Pitout, F., Blelly, P.-L., & Alcayde, D. (2013). High-latitude ionospheric response to the solar eclipse of 1 August 2008: EISCAT observations and TRANSCAR simulation. *Journal of Atmospheric and Solar-Terrestrial Physics*, *105*, 336–349. https://doi.org/10.1016/j.jastp.2013.02.004

Qian, L., Burns, A. G., Emery, B. A., Foster, B., Lu, G., Maute, A., et al. (2014). The NCAR TIE-GCM: A community model of the coupled thermosphere/ionosphere system. In *Modeling the ionosphere–thermosphere system* (pp. 73–83). John Wiley & Sons, Ltd. https://doi.org/10.1002/9781118704417.ch7

Richmond, A. D., Ridley, E. C., & Roble, R. G. (1992). A thermosphere/ionosphere general circulation model with coupled electrodynamics. *Geophysical Research Letters*, *19*(6), 601–604. https://doi.org/10.1029/92GL00401

Ridley, E. C., Dickinson, R. E., Roble, R. G., & Rees, M. H. (1984). Thermospheric response to the June 11, 1983, solar eclipse. *Journal of Geophysical Research*, *89*(A9), 7583–7588. https://doi.org/10.1029/JA089iA09p07583

Rishbeth, H. (1968). Solar eclipses and ionospheric theory. *Space Science Reviews*, *8*(4), 543–554.

Rishbeth, H., & Garriott, O. K. (1969). *Introduction to ionospheric physics* (Chap. IV, pp. 126–159). San Diego, CA: Academic Press.

Roble, R. G., Emery, B. A., & Ridley, E. C. (1986). Ionospheric and thermospheric response over Millstone Hill to the May 30, 1984, annular solar eclipse. *Journal of Geophysical Research*, *91*(A2), 1661–1670. https://doi.org/10.1029/JA091iA02p01661

Roble, R. G., Ridley, E. C., Richmond, A. D., & Dickinson, R. E. (1988). A coupled thermosphere/ionosphere general circulation model. *Geophysical Research Letters*, *15*(12), 1325–1328. https://doi.org/10.1029/GL015i012p01325

Salah, J. E., Oliver, W. L., Foster, J. C., Holt, J. M., Emery, B. A., & Roble, R. G. (1986). Observations of the May 30, 1984, annular solar eclipse at Millstone Hill. *Journal of Geophysical Research*, *91*(A2), 1651–1660. https://doi.org/10.1029/JA091iA02p01651

Sharma, S., Dashora, N., Galav, P., & Pandey, R. (2010). Total solar eclipse of July 22, 2009: Its impact on the total electron content and ionospheric electron density in the Indian zone. *Journal of Atmospheric and Solar-Terrestrial Physics*, *72*(18), 1387–1392. https://doi.org/10.1016/j.jastp.2010.10.006

Stubbe, P. (1970). The F-region during an eclipse—A theoretical study. *Journal of Atmospheric and Terrestrial Physics*, *32*(6), 1109–1116. https://doi.org/10.1016/0021-9169(70)90121-2

Tsai, H. F., & Liu, J. Y. (1999). Ionospheric total electron content response to solar eclipses. *Journal of Geophysical Research*, *104*(A6), 12,657–12,668. https://doi.org/10.1029/1999JA900001

Wang, W. (1998). A thermosphere ionosphere nested grid (TING) model, (PhD thesis). University of Michigan.

Weimer, D. R. (2005). Improved ionospheric electrodynamic models and application to calculating joule heating rates. *Journal of Geophysical Research*, *110*, A05306. https://doi.org/10.1029/2004JA010884

Zhang, S.-R., Erickson, P. J., Goncharenko, L. P., Coster, A. J., Rideout, W., & Vierinen, J. (2017). Ionospheric bow waves and perturbations induced by the 21 August 2017 solar eclipse. *Geophysical Research Letters*, *44*, 12,067–12,073. https://doi.org/10.1002/2017GL076054

Zhang, S.-R., Foster, J. C., Holt, J. M., Erickson, P. J., & Coster, A. J. (2012). Magnetic declination and zonal wind effects on longitudinal differences of ionospheric electron density at midlatitudes. *Journal of Geophysical Research*, *117*, A08329. https://doi.org/10.1029/2012JA017954